

# Land Cover Classification from Remote Sensing Images Based on Multi-Scale Fully Convolutional Network

Rui Li, Shunyi Zheng, and Chenxi Duan

**Abstract**—Land cover classification plays an important role in land resource management, cultivated area evaluation, and economic assessment. Convolutional neural network (CNN) is an effective method to extract identifying information from remote sensing images. Nevertheless, the frequently-used single-scale convolution kernel limits the scope of information extraction. In this paper, a Multi-Scale Fully Convolutional Network (MSFCN) with multi-scale convolutional kernel is proposed to exploit discriminative representations from two-dimensional (2D) satellite images. Meanwhile, when it comes to spatio-temporal images, the mainstream 2D fully convolutional neural network (FCN) collapses the temporal dimension when exploiting the spatial features, which ruins the time series information contained in multi-temporal satellite images. Hence, we expand our MSFCN to three-dimension using three-dimensional (3D) CNN, which is capable of harnessing the time series interaction of each land cover category from the reshaped spatio-temporal remote sensing images. What is more, a channel attention block (CAB) and a global pooling module (GPM) are included to enhance the channel consistency and global contextual consistency. Experiments conducted on two spatial datasets and two spatio-temporal datasets both demonstrate the effectiveness of our MSFCN.

**Index Terms**—spatio-temporal remote sensing images, multi-scale fully convolutional network, land cover classification

## I. INTRODUCTION

Land cover classification is a foundational technology for land resource management, cultivated area evaluation, and economic assessment, which is significant for homeland security and national economic stability [1]. Conventionally, large-scale field surveys are the primary method to obtain the condition of land use and land cover. Despite the outcomes of surveys are in high quality, the investigative procedures are time-consuming and labor-intensive. Meanwhile, the information about the geographical distribution of land cover is often missing [2, 3].

As a significant Earth observation technology, remote sensing is able to capture Earth’s surface images via sensors on aircrafts or satellites without physical contact [4]. The optical

remote sensing is a major branch of remote sensing and has been applied in many fields including super-resolution land cover mapping [5], drinking water protection [6], and object detection [7]. Profiting from the abundant remote sensing images, scholars have increasingly focused on automatic land cover classification using satellite images [8, 9].

Generally, remote sensing classification models consist of two procedures, feature engineering and classifier training; the former is aimed at transforming spatial, spectral, or temporal information into discriminative feature vectors, and the latter is designed to train a general-purpose classifier to classify the feature vectors into the correct category.

When it comes to land cover classification, vegetation indices are one genre of frequently-used features extracted from multi-spectral/multi-temporal images to manifest physical properties of land cover. The normalized difference vegetation index (NDVI) [10] and soil-adjusted vegetation index (SAVI) [11] highlight vegetation over other of land resources, while the normalized difference bareness index (NDBaI) [12] and the normalized difference bare land index (NBLI) [13] emphasize bare land, and the normalized difference water index (NDWI) [14] and modified NDWI (MNDWI) [15] indicate water.

Meanwhile, the remote sensing community has tried to design assorted classifiers from diverse perspectives, from orthodox methods such as logistic regression [16], distance measure [17] and clustering [18], to advanced methods including support vector machine (SVM) [19], random forest (RF) [20], artificial neural network (ANN) [21], and multi-layer perceptron (MLP) [22]. Since extraction of the geographical distribution of land cover requires pixel-based image classification, how to precisely refine pixel features is the core of these classifiers. However, the high dependency on manual descriptors restricts the flexibility and adaptability of these methods.

Deep Learning (DL) is powerful to automatically capture nonlinear and hierarchical features and has influenced many domains such as computer vision (CV) [23], natural language processing (NLP) [24], as well as automatic speech recognition (ASR) [25]. As a typical classification task, there are many DL

---

This work was supported in part by the National Key R&D Program of China (No. 2017YFB0503004) and National Natural Science Foundations of China (No. 41671452). (*Corresponding author: Rui Li.*)

R. Li and S. Zheng are with School of Remote Sensing and Information Engineering, Wuhan University, Wuhan 430079, China (e-mail: [lironui@whu.edu.cn](mailto:lironui@whu.edu.cn); [syzzheng@whu.edu.cn](mailto:syzzheng@whu.edu.cn)).

C. Duan is with the State Key Laboratory of Information Engineering in Surveying, Mapping, and Remote Sensing, Wuhan University, Wuhan 430079, China; [chenxiduan@whu.edu.cn](mailto:chenxiduan@whu.edu.cn) (e-mail: [chenxiduan@whu.edu.cn](mailto:chenxiduan@whu.edu.cn)).

methods that have been introduced to land cover classification. Compared to vegetation indices which only consider finite bands, DL methods can harness a variety of information including periods, spectrums, and the interactions between different kinds of land cover.

Zhong et al. [26] exploited temporal feature using a one-dimensional (1D) CNN to recognize intricate seasonal dynamics of economic crops and lessened the dependency on hand-crafted feature engineering for multi-temporal crop classification. Pelletier et al. [8] proposed a temporal CNN for satellite image time series and proved the significance of harnessing the information both in spectral dimension and temporal dimension when implementing the convolutions. Based on fine-tuned CNN, Tong et al. [27] combined hierarchical segmentation and patch-wise classification for land cover classification. Semantic segmentation, an important and common task in computer vision, has been applied to land cover classification using satellite images. Inspired by the progress in the encoder-decoder Fully Convolutional Network (FCN) framework like U-Net, Stoian et al. [28] proposed a Fine Grained U-Net architecture for sparse annotation images captured by Sentinel-2. Cao et al. [29] incorporated the U-Net and ResNet to classify the tree species using high-resolution images.

Even though the encoder-decoder FCN framework [30-32] has been a basic structure for land cover classification [33-35], the single-scale convolution kernel limits the scope of information extraction. To cope with this issue, we propose a Multi-Scale Fully Convolutional Network based on encoder-decoder FCN structure to exploit both local and global features from satellite images for land cover classification. In each layer of the encoder, we design two branches with convolutional layers in different kernel sizes to capture multi-scale features. In addition, a channel attention block and a global pooling module [36] are adopted to enhance the channel consistency and global contextual consistency.

Currently, spatio-temporal satellite images, bolstered by their increasing attainability, are at the forefront of a comprehensive effort towards automatic Earth monitoring by international agencies [37]. However, when utilizing the 2D CNN to extract features from spatio-temporal satellite images, the temporal dimensions of the extracted features generated by the convolution layer must be averaged and devastated to a scalar, which collapses the time series information contained in multi-temporal images. To handle this problem, many studies have been conducted motivated by the progress of NLP, which should model temporal sequences of language. Rußwurm et al. [38, 39] adapted sequence encoders to model temporal sequence of Sentinel 2 images, and alleviated the demand of humdrum and cumbersome cloud-filtering. Interdonato et al. [40] designed a two-branch architecture, a RNN branch to extract temporal features and a CNN branch to extract spatial features, for time series classification. By incorporating both CNN and RNN, Rustowicz et al. [41] designed a 2D U-Net + CLSTM model for spatio-temporal satellite images. Meanwhile, for embedding time-sequences, Transformer architecture was also introduced into land cover classification using spatio-

temporal satellite images by Garnot et al. [37]. All these attempts have made encouraging progress and broadened the boundaries of land cover classification.

Meanwhile, the advent of 3D CNN solves the above-mentioned dilemma from another perspective. Unlike traditional 2D CNN which operates on 2D images, 3D CNN implements convolutional operation on three dimensions, which naturally fits feature extraction from spatio-temporal satellite images and other data represented in 3D format. Thus, 3D CNN has been utilized for video understanding [42], point clouds representation [43], 3D object detection based on light detection and ranging (LiDAR) data [44], hyperspectral images classification [45], and multi-temporal images segmentation [46]. As the temporal or spectral dimensions are generally not considered independently in conventional computer vision tasks, the usage scenarios of 3D CNN are less than 2D CNN, which affects the popularization of 3D CNN for land cover classification using multi-temporal images. However, as to remote sensing images which comprise abundant temporal, dynamic, or spectral information, like the whole crop growth cycle contained in the temporal dimension, 3D CNN is a superexcellent method to extract these features.

Using multi-temporal images, Ji et al. [46] designed a 3D-CNN-based segmentation model for crop classification. As the temporal dimension is reserved, the performance of the model surpassed the 2D-CNN-based methods and other traditional classifiers. However, as 3D CNN is a computationally intensive operation, the pixel-by-pixel segmented procedure of their work requires numerous computational resources. Thus, based on the idea of semantic segmentation, Ji et al. [36] proposed a novel 3D encoder-decoder FCN framework with global pooling and attention mechanism (3D FGC), which was able to capture feature maps from the whole input and improves both the accuracy and the efficiency.

Based on the above-mentioned insight and progress, we extend our Multi-Scale Fully Convolutional Network to three-dimension based on 3D CNN for land cover classification using spatio-temporal satellite images. To verify the effectiveness, we compare the performance of 2D MSFCN with SegNet [31], FC-DenseNet [47], U-Net [30], Attention U-Net [48] and FGC [36] and the performance of 3D MSFCN with 1D U-Net, 2D U-Net [30], 3D U-Net [30], Conv-LSTM [38] and 3D FGC [36]. In addition, we expand 2D Attention U-Net [48] to 3D and contrast its capability to MSFCN. The major contributions of this paper could be listed as follows:

- 1) To expand the scope of information extraction in the spatial domain, we designed a multi-scale convolutional block (MSCB), which is able to capture the local and global features of the input respectively.
- 2) Based on MSCB, we proposed a Multi-Scale Fully Convolutional Network (MSFCN) with channel attention block and global pooling module, and extend MSFCN to 3D for spatio-temporal satellite images.
- 3) We verify the effectiveness of the channel attention block which enhances the channel consistency and the global pooling module which boosts the global contextual consistency.

- 4) The 3D version Attention U-Net is designed, and the experiments validate its validity for land cover classification using spatio-temporal satellite images, especially when compared with 3D U-Net.
- 5) A series of quantitative experiments on two spatial datasets and two spatio-temporal datasets show the effectiveness of proposed MSFCN.

The remainder of this paper is arranged as follows: In Section 2, taking 3D MSFCN as an example, we illustrate the detailed structure of proposed framework. The experimental results are provided and analyzed in Sections 3. Finally, in Section 4 we draw a conclusion of the entire paper.

## II. METHODOLOGY

### A. Feature Extraction using 3D CNN

3D CNN is capable of capturing spatial and temporal features simultaneously, and Batch Normalization (BN) layer [49] is often appended to improve numerical stability. Thus, we consider 3D CNN with a BN layer as an example to elaborate the mechanism of 3D CNN. Supposing that the size of input 3D feature maps is expressed as  $(t \times h \times w, c)$ , and the shape of the convolution kernel is  $(k_t \times k_h \times k_w)$ , where  $t, h, w$ , and  $c$  denote the dimension of time series, height, width, and channels. The convolution operations are implemented between the convolution kernel and sliding windows in the shape of  $(k_t \times k_h \times k_w)$ , and the obtained values constitute the output 3D feature maps. Another important parameter, stride, determines the distance of width and height traversed per slide of the sliding windows. A diagrammatic sketch with one kernel can be seen in Fig. 1. Concretely, the operation of 3D CNN can be formulized as:

$$\begin{aligned} & \mathbf{x}_{i,j}^{t,h,w} \\ &= \sum_m \sum_{p=0}^{T_i-1} \sum_{q=0}^{H_i-1} \sum_{r=0}^{W_i-1} \mathbf{W}_{i,j,m}^{p,q,r} \mathbf{x}_{i-1,m}^{(t+p),(h+q),(w+r)} + b_{i,j} \end{aligned} \quad (1)$$

where  $\mathbf{x}_{i,j}^{t,h,w}$  denotes the  $j$ th feature cube at position  $(t, h, w)$  in the  $i$ th layer,  $m$  means the feature maps generated by the  $(i-1)$ th layer.  $\mathbf{W}_{i,j,m}^{p,q,r}$  represents the column weight of the  $m$ th feature cube at position  $(p, q, r)$ .  $b_{i,j}$  is the  $j$ th feature cube in the  $i$ th layer's bias items of the filter.  $T_i$  means the convolution kernel along the temporal dimension of input spatio-temporal satellite images, while  $H_i$  and  $W_i$  respectively express the height and width of the kernel in the spatial dimension.

Then, the generated 3D feature maps  $\mathbf{x}_i$  is fed into the BN layer and normalized as:

$$\hat{\mathbf{x}}_i = \frac{\mathbf{x}_i - E(\mathbf{x}_i)}{\sqrt{\text{Var}(\mathbf{x}_i) + \epsilon}} \quad (2)$$

$$\mathbf{y}_i = \sigma(\gamma_i \hat{\mathbf{x}}_i + \beta_i) \quad (3)$$

where  $\mathbf{y}_i$  is the output of the BN layer.  $\text{Var}(\cdot)$  and  $E(\cdot)$  represent the variance function and expectation of the input.  $\epsilon$  is a small constant to maintain numerical stability.  $\gamma$  and  $\beta$  are two trainable parameters, and the normalized result  $\hat{\mathbf{x}}_i$  can be

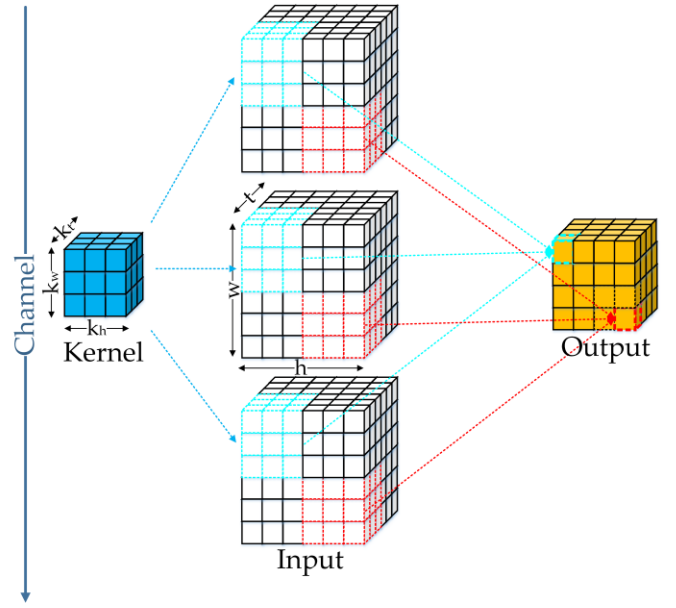


Fig. 1. 3D convolution indicates convolution operator is implemented in three directions (i.e. two spatial directions and a temporal direction) sequentially. Both the input feature maps and the output feature maps are 3D tensors.

scaled by  $\gamma$  and shifted by  $\beta$ .  $\sigma(\cdot)$  denotes the activation function, which is set as ReLU in our model.

As the quality of extracted features limits the performance of the model and the convolution kernel size determines the receptive field, how to design the size of the convolution kernel is the crux of the network.

### B. Multi-Scale Convolutional Block

Generally, the larger convolution kernel size means the larger receptive field and the more global vision, which augments the scope of areas observed in the image. Conversely, the decrease in the size of the convolution kernel would shrink the receptive field and obtain the local vision. However, both the global visual patterns and the local visual patterns contain visual features. Thus, an evident imperfection of the fully convolutional neural network is that the convolutional kernels are in the same size, which means the receptive field of a convolutional layer is constant. As can be seen in Fig. 2(a), the conventional convolutional block used in FCN usually contains two stacked 3D CNN with the activation function. To expand the receptive field, in MSFCN, we design a multi-scale convolutional block (MSCB) to exploit the global and local features simultaneously.

The structure of the multi-scale fully convolutional layer can be seen in Fig. 2(b). Similarly, supposing the input 3D feature maps is in the shape of  $(t \times h \times w, c)$ , where the  $t, h, w$ , and  $c$  represent the time series, height, width, and channels of the input. The top branch of the block contains two stacked  $(3 \times 3 \times 3)$  convolution layers, and the receptive field of two stacked  $(3 \times 3 \times 3)$  convolution layers are equivalent to a  $(5 \times 5 \times 5)$  convolution layer, which can be seen from Fig. 3. Thus, the top branch is capable of capturing more global visual patterns. Meanwhile, the bottom branch of the block harnesses

a single  $(3 \times 3 \times 3)$  convolution layer which exploits local visual patterns.

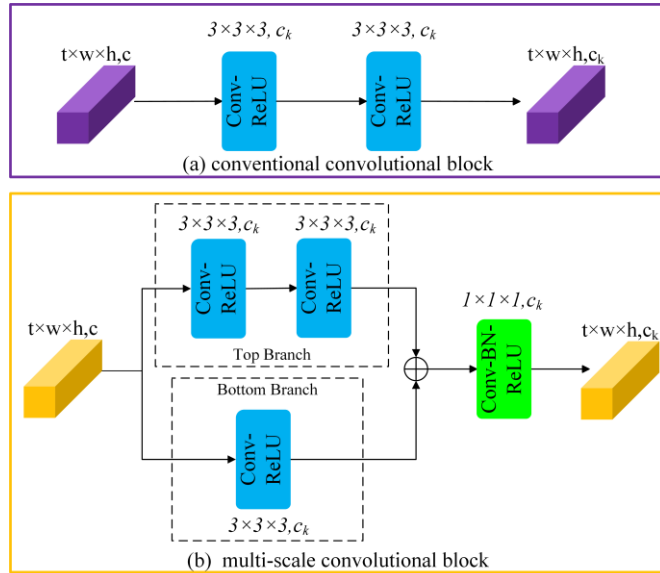


Fig. 2. Comparison of (a) conventional convolution block and (b) multi-scale convolution block.

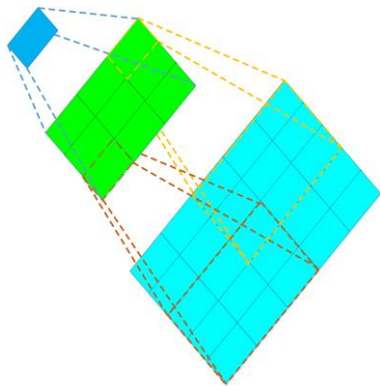


Fig. 3. The receptive field of two stacked  $(3 \times 3)$  convolution layers is equivalent to a  $(5 \times 5)$  convolution layer, and the same is true of 3D CNN.

Subsequently, the add operation is implemented between the outputs of the top branch and the bottom branch, and obtains the feature maps with the size of  $(t \times h \times w, c_k)$ . Finally, the extracted feature maps are fed into a  $(1 \times 1 \times 1)$  convolution layer with BN layer to further increase the nonlinear characteristics and characterization capabilities of the block.

### C. Channel Attention Block and Global Pooling Module

In the FCN framework, the output of the convolution operator is a score map, which indicates the probability of each class at each pixel. And to attain the final score map, all channels of feature maps are simply summed as:

$$y_n = F(x; \omega) = \sum_{i=1, j=1, k=1}^D \omega_{i,j,k} x_{i,j,k} \quad (4)$$

$\omega$  denotes the convolution kernel.  $x$  represents the feature maps generated by the network.  $D$  is the set of pixel positions. And  $n \in \{1, 2, \dots, N\}$ , where  $N$  indicates the number of channels. Then the prediction probability is generated as:

$$\delta_i(y_n) = \frac{\exp(y_n)}{\sum_{j=1}^K \exp(y_j)} \quad (5)$$

where  $y$  denotes the output of the network, and  $\delta$  indicates the prediction probability. Obviously, the category with the highest probability is the final predicted label which can be deduced by Equation 4 and Equation 5. Equation 4 impliedly indicates that all channels share equal weights. However, the features generated by different stages own different levels of discrimination, which causes different consistency in prediction.

Supposing the prediction label is  $y_0$  and that the corresponding true label is  $y_1$ , we can modify the highest probability value from  $y_0$  to  $y_1$  by introducing a parameter  $\alpha$ :

$$\bar{y} = \alpha y = \begin{bmatrix} \alpha_1 \\ \vdots \\ \alpha_N \end{bmatrix} \cdot \begin{bmatrix} y_1 \\ \vdots \\ y_N \end{bmatrix} = \begin{bmatrix} \alpha_1 \omega_1 \\ \vdots \\ \alpha_N \omega_N \end{bmatrix} \times \begin{bmatrix} x_1 \\ \vdots \\ x_N \end{bmatrix} \quad (6)$$

in which  $\alpha = \text{Sigmoid}(x; w)$  and  $\bar{y}$  is the new prediction label of the network. As can be seen from Equation 6, the  $\alpha$  value weights the feature maps  $x$  and enhances the discriminative features and restrains the indiscriminate features. The channel attention block is designed based on the above-mentioned insight [50, 51] and is expanded to the 3D version [36].

The structure of the CAB can be seen in Fig. 4, whose input is the concatenated feature maps extracted by the encoder and decoder. First, a 3D global average pooling layer in CAB exploits the global context of the input, and sequentially two  $(1 \times 1 \times 1)$  convolution layers with ReLU and sigmoid activation function adaptively realign the channel-wise dependencies. The weight vector generated by CAB models the relative significance between the channel-wise features and enhances the discriminability about features. Then a multiplication operation and an addition operation are operated between the output vector and the input feature maps. Finally, the last  $(1 \times 1 \times 1)$  convolution layer is designed to generate globally consistent spatio-temporal feature maps. Through re-weighting the channel-wise features, 3D channel attention block (CAB) fuses the spatio-temporal features between the encoder and the decoder.

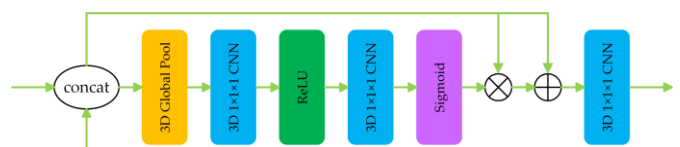


Fig. 4. The structure of the channel attention block (CAB).

Meanwhile, context is a salutary information which can be used to enhance the performance on segmentation and detection using deep learning [52]. As for land cover classification, local semantic information contained in per pixel is often equivocal. And by taking contextual information into consideration, the semantic information will be enhanced. Global average pooling is proved to be a good method to capture the global contextual prior [52]. Based on the idea that the spatio-temporal consistency can be enhanced by a global average pooling layer on the highest level of the encoder (i.e. the top semantic layer) [51], the global pooling module (GPM) is elaborately designed [36], which can be seen in Fig. 5. Meanwhile, with global

spatio-temporal consistency, the GPM transforms the feature maps at highest level of the encoder to the corresponding feature maps of the decoder. Just like the CAB, the effect of GPM is reweighting feature maps, which also can be seen as an attention mechanism.

The structure of the GPM can be seen in Fig. 5. First, the input feature maps are fed into a  $(1 \times 1 \times 1)$  convolution layer. Then, a 3D global average pooling and a  $(1 \times 1 \times 1)$  convolution layer with sigmoid activation function are attached. Finally, a multiplication operation and an addition operation are implemented between the generated vector and the output obtained by the first convolution layer, and the final output is processed by the last  $(1 \times 1 \times 1)$  convolution layer to acquire the highest layer of the decoder.

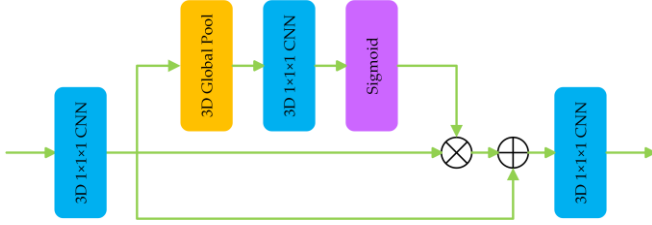


Fig. 5. The structure of the global pooling module (GPM).

#### D. Network Architecture

Based on the 3D CNN, the multi-scale convolutional block, the channel attention block, and the global pooling module, we construct the MSFCN for land cover classification from satellite images, which can be seen in Fig. 6. The encoder of the MSFCN comprises four multi-scale convolutional blocks with the output channels as 32, 64, 128, and 256 respectively, and the number of layers and channels will be discussed in Section III.F. After each multi-scale convolutional block, the max-pooling layer with  $(1 \times 2 \times 2)$  kernel is applied, which reserves the temporal information and condenses the spatial information. At the highest layer of the encoder, the GPM is utilized to enhance the global spatio-temporal consistency. Then, using CAB, the feature maps from the encoder and decoder are fused, and the output of each layer in decoder is sequentially restored up to the input size via the transposed convolution layer with  $(1 \times 2 \times 2)$  kernel. After each transposed convolution layer, a  $(3 \times 3 \times 3)$  convolution layer is attached to avoid the checkerboard pattern generated by the transposed convolution. In the end, the final 3D feature maps are fed into a  $(t \times 3 \times 3)$  convolution layer and a  $(1 \times 1 \times 1)$  convolution layer to coalesce time dimension and generate 2D segmentation maps.

The cross-entropy loss function is used as quantitative evaluation and backpropagation index to measure the disparity between the obtained 2D segmentation maps and ground truth, which is defined as:

$$loss_{i,j} = - \sum_k q_{i,j,k} \log p_{i,j,k} \quad (7)$$

$$loss = \frac{1}{N} \sum_i \sum_j loss_{i,j} \quad (8)$$

where  $p_{i,j}$  is the predicted category probability distribution of pixel  $(i,j)$ ,  $q_{i,j}$  is the actual category probability distribution of pixel  $(i,j)$ ,  $k$  represents the number of classes, and  $N$  denotes the number of pixels.

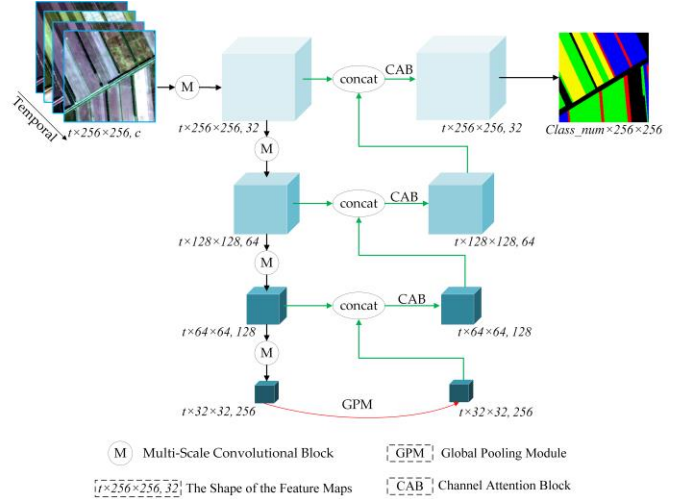


Fig. 6. The structure of the proposed MSFCN network.

### III. EXPERIMENTAL RESULTS

This section first introduces the datasets and experimental settings to verify the effectiveness of MSFCN, and then compares the performance between different frameworks.

#### A. Datasets

The effectiveness of 2D MSFCN is verified using Wuhan Dense Labeling Dataset (WHLDL) [53, 54] and Gaofen Image Dataset (GID) [30] which can be seen in Fig.7 and Fig. 8, and the effectiveness of 3D MSFCN is verified using two Gaofen 2 (GF2) spatio-temporal satellite images [36], which can be seen in Fig. 9.

WHLDL contains 4940 RGB images in the size of  $256 \times 256$  captured by Gaofen 1 Satellite and ZY-3 Satellite over Wuhan urban area. By image fusion and resampling, the images resolution is reach to 2m/pixel. The images contained in WHLDL are labeled with six classes, i.e. bare soil, building, pavement, vegetation, road, and water.

GID contains 150 RGB images in the size of  $7200 \times 6800$  captured by Gaofen 2 Satellite over 60 cities in China. Each image covering a geographic region of  $506 \text{ km}^2$ . The images contained in GID are labeled with six classes, i.e. build-up, forest, farmland, meadow, water, and others. However, as we don't have enough computing resources to cope with such extremely enormous pixels, we just select 15 images contained in GID. The principle of selection is to cover whole six classes. And the serial number of the selected images will be released with our open source code <sup>1</sup>.

<sup>1</sup> <https://github.com/lironui/Multi-Scale-Fully-Convolutional-Network>.

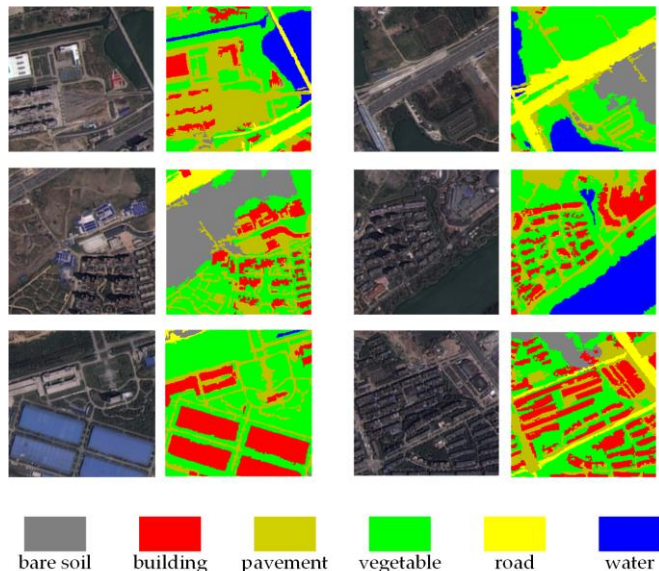


Fig. 7. Examples of WHDLD images and their corresponding ground truth.

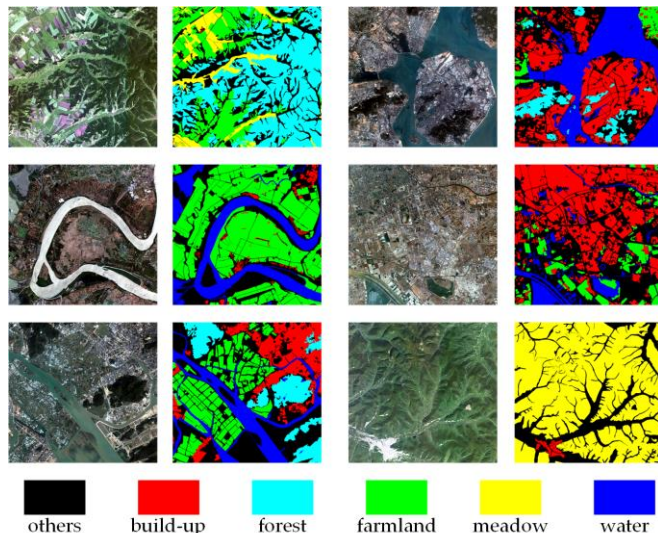


Fig. 8. Examples of GID images and their corresponding ground truth.

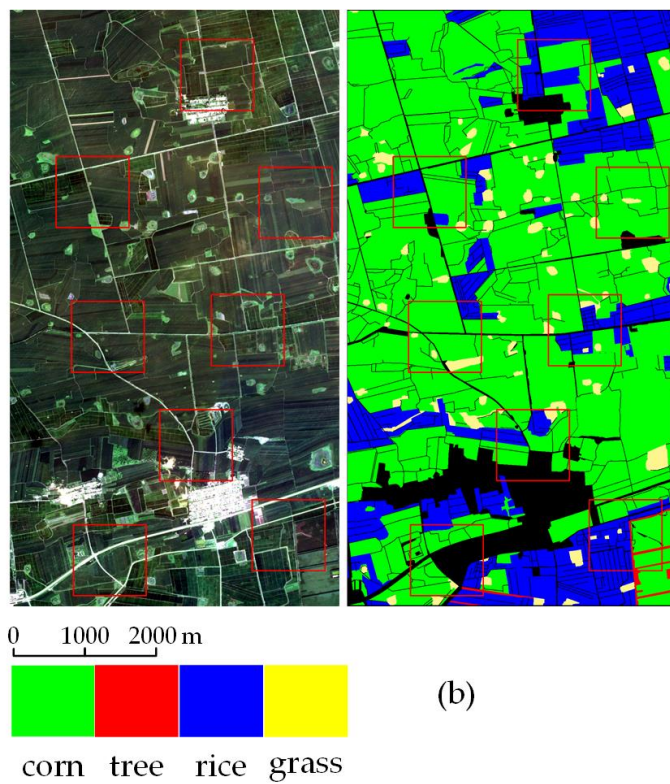
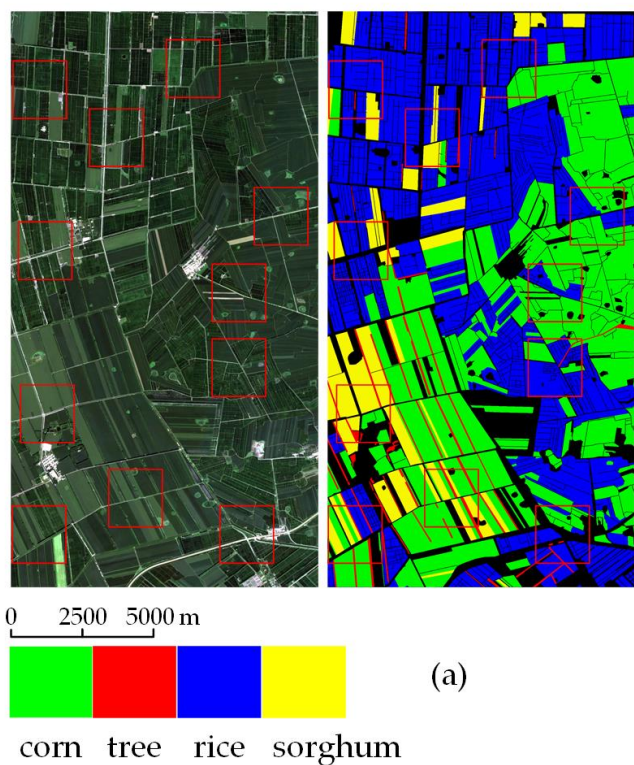


Fig. 9. GF2 datasets gathered in (a) 2015, and (b) 2017. Each dataset owns four crop species labelled in different color, and black pixels represent the label information are absent. Patches indicated in red rectangles were utilized to train the network and the remainder to prediction.

The two spatio-temporal satellite datasets that own four bands (red, green, blue, and near infrared) in 4m ground resolution were gathered in 2015 and 2017, respectively. For 2015 dataset, there are four images gathered in June, July, August, and September in the year of 2015, and  $2652 \times 1417$  pixels of each image. The 2017 dataset comprises seven images with  $2102 \times 1163$  pixels captured in June, July, August, September, October, November, and December in the year of 2017. Two GF2 datasets are preprocessed with the quick atmospheric correction [55] and geometrical rectification.

### B. Experimental Setting

To evaluate the effectiveness of 2D MSFCN, SegNet [31], FC-DenseNet57 (Tiramisu) [47], U-Net [30], Attention U-Net (U-NetAtt) [48] and FGC [36] are taken into comparison. And the performance of 3D MSFCN are compared with 1D U-Net, 2D U-Net [30], 3D U-Net [30], Conv-LSTM [38] and 3D FGC [36]. In addition, we expand 2D Attention U-Net [48] to 3D and contrast its capability with MSFCN.

All of the models are implemented with PyTorch, and the

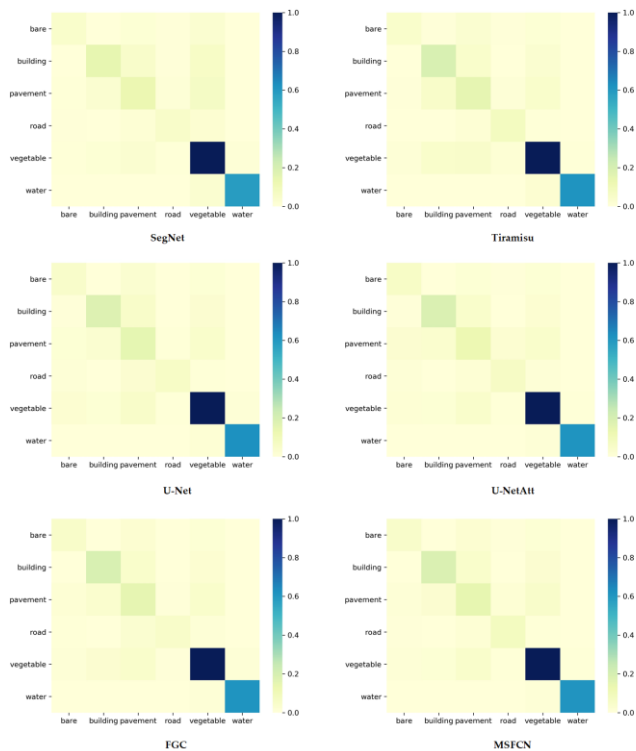


Fig. 10. Heat Maps of different methods on WHDL D.

optimizer is set as Adam with 0.0001 learning rate. The batch size is set as 16 for WHDL D and GID, and 4 for GF2 spatio-temporal satellite images. All the experiments are implemented on a single NVIDIA GeForce RTX 2080ti GPU with 11 GB RAM.

For WHDL D, we randomly select 60% images as training set, 20% images as validation set, and the rest 20% images as test set. For GID, we separately partition each image into non-overlap patch sets with the size of  $256 \times 256$ , and just discard the pixels on the edges which cannot be divisible by 256. Thus, 10920 patches are obtained. Then we randomly select 60% patches as training set, 20% patches as validation set, and the rest 20% patches as test set. And the training sets of WHDL D and GID are augmented by horizontal axis flipping, vertical axis flipping, color enhancement, Gaussian blur and random noise. When training the network, if the accuracy in validation set is no longer increasing for 10 epochs, then we would terminate the training process early to restrain overfitting. The number of training, validation and test pixels per class for WHDL D and GID is provided in Table I.

For two spatio-temporal satellite images, the samples in each category are severely imbalanced. Thus, we selected portion of the images which contains samples of all the categories to train the network, which is indicated in red rectangles in Fig. 9. Since pixels in these two datasets are not abundant, we enlarge the images in 2015 dataset to the size of  $2816 \times 1536$  and the images in 2017 dataset to the size of  $2304 \times 1280$  by zero-padding, and then segment each image into non-overlap patch sets in the size of  $256 \times 256$  to evaluate prediction accuracy. Of course, the selected portion for training is also set as zero to avoid data leakage. The number of training and test pixels per

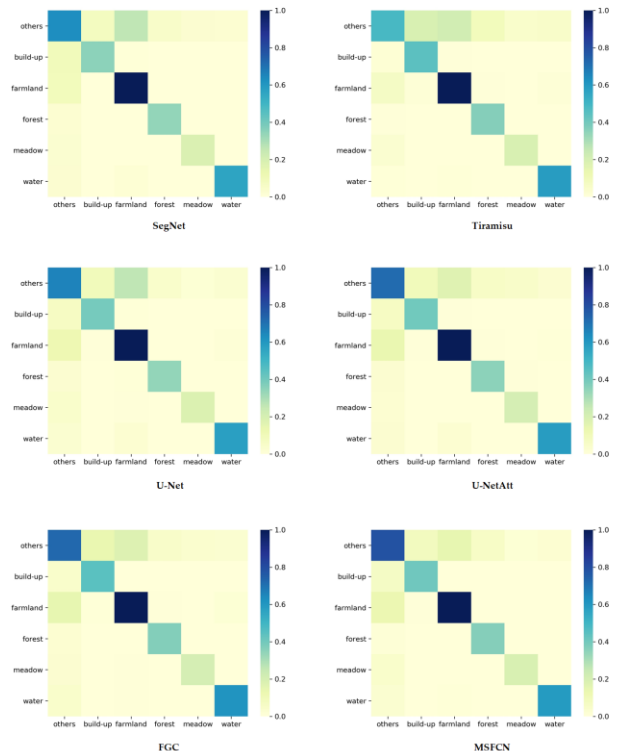


Fig. 11. Heat Maps of different methods on GID.

table

	Train	Val	Test	
WHDL D	bare	7746403	2475482	2854410
	building	21848819	7135568	6917771
	pavement	22842445	7671979	6782834
	road	8225161	2850179	2869957
	vegetable	87444443	28505640	28859223
	water	46141433	16110720	16465373
GID	others	125858447	40426710	40061365
	build-up	49528719	16603346	17203079
	farmland	125542298	41351598	40884984
	forest	37555494	12302122	13716761
	meadow	25657841	9335581	8437873
	water	65249073	23111267	22826562

2015	Train	Test	2017	Train	Test
rice	253286	1069586	rice	93931	356085
corn	198585	1064487	corn	320895	1206244
sorghum	102649	193686	grass	15140	63117
tree	17410	57677	tree	3941	7787

class is provided in Table II. Each model is trained 100 epochs on the training set, and then verified on the test set.

For each dataset, the overall accuracy (OA), average accuracy (AA), Kappa coefficient (K), mean Intersection over Union (mIoU), Frequency Weighted Intersection over Union (FWIoU), and F1-score (F1) are adopted as evaluation indexes. Given the predicted segmentation maps and ground truth, the IoU indicates the size of their intersection divided by the size of their union. The mIoU averages the IoU of every category, and the FWIoU weights IoU of each category by the frequency. We select mIoU as the main indicator, as it reflects both the overall accuracy (OA) and the consistency degree (Kappa), and is

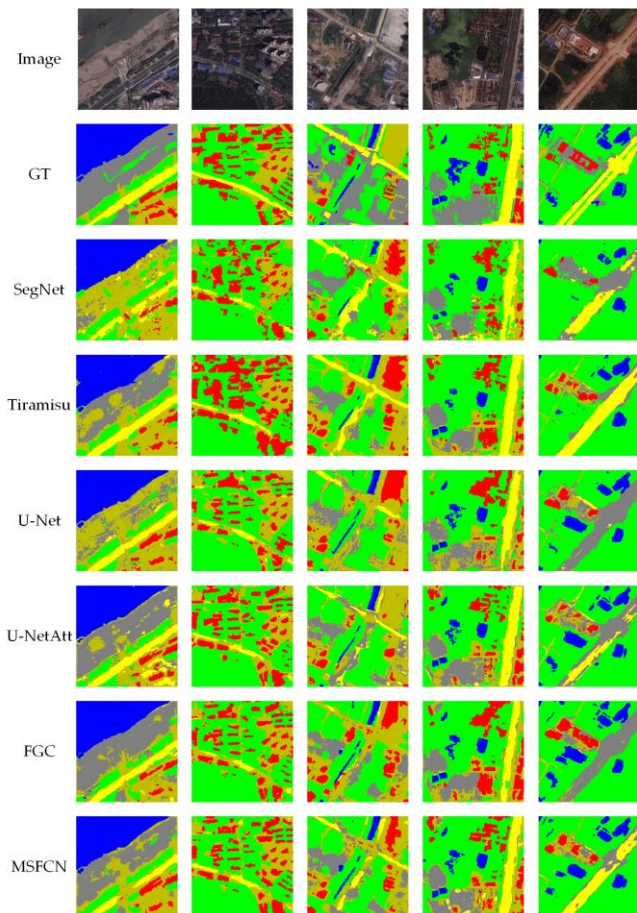


Fig. 12. Land cover classification results of the method proposed and comparisons on WHDL D.

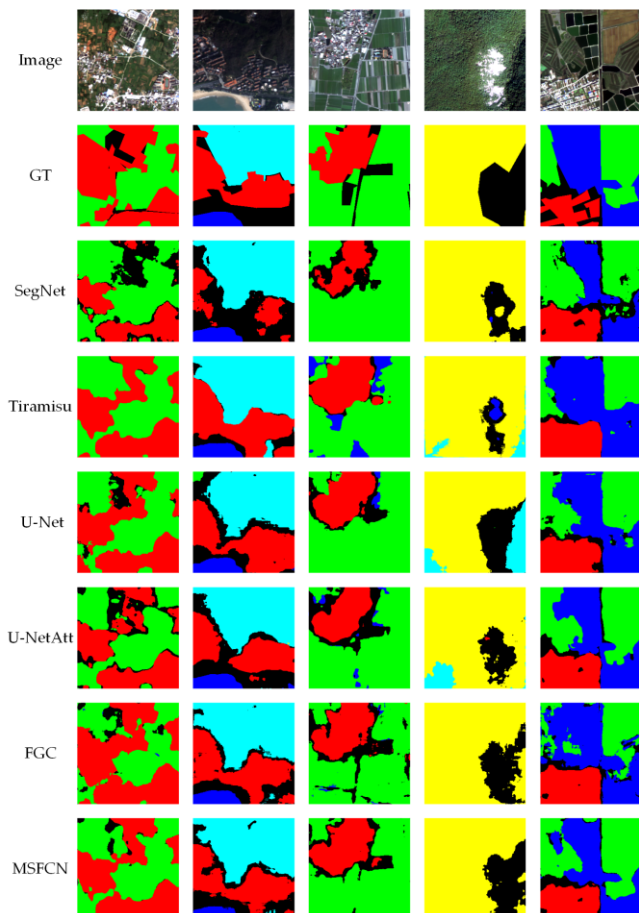


Fig. 13. Land cover classification results of the method proposed and comparisons on GID.

becoming a frequently-used indicator for land cover segmentation [35, 56, 57].

### C. Results on WHDL D and GID

The experimental results of different methods on WHDL D and GID are demonstrated in Table III and Table IV. The performance of proposed MSFCN transcends other algorithms in all quantitative evaluation indexes, which can be seen from tables.

TABLE III  
THE EXPERIMENTAL RESULTS ON WHDL D DATASET.

Method	OA	AA	K	mIoU	FWIoU	F1
SegNet	80.229	63.787	71.403	52.940	68.876	66.529
Tiramisu	82.188	70.712	74.903	58.167	72.243	71.276
U-Net	81.830	67.724	74.422	55.706	72.450	68.567
U-NetAtt	82.602	69.738	75.484	56.918	73.474	69.622
FGC	82.975	68.855	75.927	57.368	73.540	70.274
MSFCN	<b>84.168</b>	<b>72.081</b>	<b>77.558</b>	<b>60.366</b>	<b>74.892</b>	<b>73.031</b>

TABLE IV  
THE EXPERIMENTAL RESULTS ON GID DATASET.

Method	OA	AA	K	mIoU	FWIoU	F1
SegNet	80.035	82.396	74.612	70.962	67.420	82.290
Tiramisu	79.467	84.008	74.377	69.032	65.627	80.716
U-Net	78.992	81.115	73.295	69.417	65.936	81.326
U-NetAtt	80.919	83.838	75.878	70.930	68.539	82.511
FGC	81.180	84.716	76.270	72.067	68.859	83.240
MSFCN	<b>83.718</b>	<b>85.544</b>	<b>79.353</b>	<b>75.127</b>	<b>72.688</b>	<b>85.378</b>

For WHDL D, the proposed MSFCN brings near 3% improvements both on mIoU and F1-score compared with FGC. And for GID dataset, the improvements are more than 3% in mIoU and more than 2% in F1-score, respectively.

Table V and Table VI summarize the per class F1-score performance of the different methods for WHDL D and GID. The proposed MSFCN obtains the best performance in most classes on WHDL D and whole classes on GID. Meanwhile, we investigate the confusion matrix between each pair of classes and we report the confusion matrix by heat maps for each competing method in Fig. 10 and Fig 11. The more visible diagonal structure (the dark blue blocks concentrated on the diagonal) indicates the more powerful capacity of distinguishing between classes. And the diagonal structure of MSFCN is more distinct than others, which proves the superiority of our framework.

TABLE V  
PER CLASS F1-SCORE PERFORMANCE ON WHDL D.

Method	bare	building	pavement	road	vegetable	water
SegNet	47.682	63.253	51.466	54.649	86.473	95.649
Tiramisu	50.313	68.918	53.576	<b>70.047</b>	88.206	96.598
U-Net	43.097	70.752	52.609	58.668	89.185	97.089
U-NetAtt	47.974	72.736	48.942	60.576	89.994	<b>97.511</b>
FGC	50.282	72.642	53.842	57.931	89.651	97.294
MSFCN	<b>52.178</b>	<b>74.499</b>	<b>55.177</b>	68.797	<b>90.024</b>	<b>97.511</b>

What is more, the number of parameters and the consumptions of calculation are also significant to assess the merit of a framework. The comparison of parameters and



TABLE VI

PER CLASS F1-SCORE PERFORMANCE ON GID.

Method	others	buildup	farmland	forest	meadow	water
SegNet	63.451	79.085	83.510	89.241	84.962	93.493
Tiramisu	57.062	79.007	85.436	87.068	83.274	92.449
U-Net	63.351	80.585	81.564	87.768	82.996	91.692
U-NetAtt	67.123	81.523	84.569	86.955	82.513	92.381
FGC	66.810	81.957	84.101	89.570	84.840	92.165
MSFCN	<b>71.536</b>	<b>83.442</b>	<b>86.907</b>	<b>90.332</b>	<b>85.752</b>	<b>94.303</b>

computational complexity between different algorithms are reported in Table VII, where ‘M’ is the abbreviation of million, the unit of parameter number, and ‘G’ is the abbreviation of Gillion (thousand million), the unit of floating point operations. And the comparison demonstrates that the design of MSFCN doesn’t bring in redundant parameters or lead to high computational complexity.

TABLE VII

THE COMPARISON OF PARAMETERS AND COMPUTATIONAL COMPLEXITY.

Method	input shape	Parameters (M)	Complexity (G)
SegNet		1.93	9.27
Tiramisu		29.45	40.29
U-Net		1.38	11.92
U-NetAtt	3×256×256	2.17	12.75
FGC		2.19	8.4
MSFCN		2.67	9.66

Some visual results generated by our method and comparisons are provided in Fig. 12 and Fig. 13.

#### D. Results on 2015 and 2017 datasets

To training the network, the inputs of the 1D U-Net are reshaped into  $(ct \times 65536)$  tensors, and the inputs of the 2D U-Net are reshaped into  $(ct \times 256 \times 256)$ , while the input of the Conv-LSTM, 3D U-Net, 3D FGC, 3D U-NetAtt and 3D MSFCN are  $(c \times t \times 256 \times 256)$  tensors, where  $c$  and  $t$  denote the number of spectral channels and time series, respectively.

The experimental results with different methods for two datasets are demonstrated in Table VIII and Table IX. Since the operation of 1D CNN destroys both the spatial dimension and temporal dimension, the performance of 1D U-Net is worst. As the operation of 2D CNN ruins the temporal dimension when extracting spatio-temporal features, the models based on 3D CNN dramatically outperform the models based on 2D CNN, which prominently demonstrates the superiority of 3D CNN. The performance of Conv-LSTM transcends 2D-based models,

TABLE VIII

THE EXPERIMENTAL RESULTS USING DIFFERENT METHODS ON 2015 DATASET.

Method	OA	AA	K	mIoU	FWIoU	F1
1D U-Net	92.302	75.017	87.339	66.745	86.581	76.114
2D U-Net	91.883	85.710	86.788	74.131	86.174	84.117
3D U-Net	96.620	85.819	94.391	82.151	93.517	88.112
3D U-NetAtt	96.272	90.662	93.876	83.441	93.143	88.947
Conv-LSTM	96.682	90.314	94.523	84.618	93.77	91.123
3D FGC	96.272	90.662	93.876	83.441	93.143	90.380
3D MSFCN	<b>97.784</b>	<b>93.275</b>	<b>96.339</b>	<b>87.753</b>	<b>95.848</b>	<b>92.971</b>

as the information contained in temporal dimension is taken into consideration. Benefitting from the utilization of attention mechanism, the 3D U-NetAtt performs better than 3D U-Net. Similarly, since the introduction of the CAB which enhances

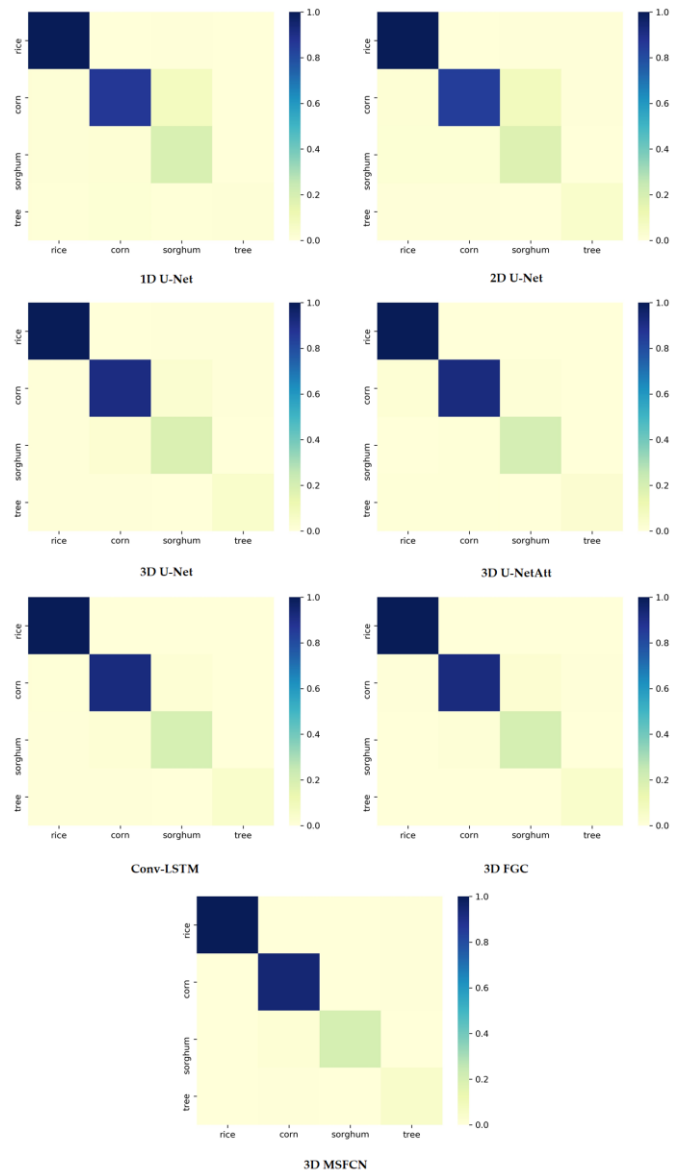


Fig. 14. Heat Maps of different methods on 2015dataset.

TABLE IX

THE EXPERIMENTAL RESULTS USING DIFFERENT METHODS ON 2017 DATASET.

Method	OA	AA	K	mIoU	FWIoU	F1
1D U-Net	95.709	74.331	89.365	66.091	92.065	75.924
2D U-Net	96.369	78.015	90.933	71.873	93.491	81.449
3D U-Net	96.662	81.836	91.851	74.375	94.252	83.497
3D U-NetAtt	97.102	82.320	93.020	75.505	94.904	84.38
Conv-LSTM	96.414	81.379	91.117	75.026	93.456	84.156
3D FGC	97.083	82.052	92.841	75.387	94.767	84.311
3D MSFCN	<b>97.132</b>	<b>85.088</b>	<b>93.039</b>	<b>77.156</b>	<b>94.880</b>	<b>86.018</b>

TABLE X

PER CLASS F1-SCORE PERFORMANCE ON 2015 DATASET.

Method	rice	corn	sorghum	tree
1D U-Net	97.743	92.968	75.965	37.781
2D U-Net	97.301	92.321	72.225	74.623
3D U-Net	98.476	95.780	82.997	75.194
3D U-NetAtt	98.369	97.055	92.721	67.642
Conv-LSTM	98.733	97.154	89.791	78.813
3D FGC	98.670	96.839	87.997	78.013
3D MSFCN	<b>99.184</b>	<b>98.203</b>	<b>94.317</b>	<b>80.180</b>

TABLE XI  
PER CLASS F1-SCORE PERFORMANCE ON 2017 DATASET.

Method	rice	corn	grass	tree
1D U-Net	96.582	97.671	58.544	50.899
2D U-Net	97.226	97.864	65.230	65.476
3D U-Net	97.868	98.115	67.790	70.215
3D U-NetAtt	97.752	98.413	74.264	67.091
Conv-LSTM	96.643	97.940	65.798	<b>76.244</b>
3D FGC	97.861	98.335	72.562	68.485
3D MSFCN	<b>98.236</b>	<b>98.586</b>	<b>77.660</b>	69.589

temporal consistency and the GPM which the global contextual consistency, the performance of FGC exceeds U-Net. Our proposed MSFCN obtains the state-of-the-art mIoU on two datasets, as both the global and local features are captured by the well-designed multi-scale convolutional blocks. Table X and Table XI report the per class F1-score performance of the different methods for 2015 dataset and 2017 dataset. The proposed MSFCN obtains the best performance in whole classes on 2015 dataset and most classes on 2017 dataset. The confusion matrix reported by heat maps for each competing method is provided in Fig. 14 and Fig. 15. And Fig. 16 demonstrates the segmentation maps on two datasets. The first three columns are from the 2015 dataset and the remainder are from the 2017 dataset. Taking the fourth column as an example, the proposed MSFCN differentiates corn (green) and grass (yellow) better than other models. Table XII provides the number of parameters and the consumptions of calculation, which illustrates the complexity of the proposed MSFCN is not unacceptable.

TABLE XII  
THE COMPARISON OF PARAMETERS AND COMPUTATIONAL COMPLEXITY.

Method	input shape	Parameters (M)	Complexity (G)
1D U-Net	16×65536	3.74	24.16
2D U-Net	16×256×256	10.86	14.18
3D U-Net		4.87	74.69
3D U-NetAtt		5.67	121.74
Conv-LSTM	4×4×256×256	0.30	77.31
3D FGC		5.32	78.51
3D MSFCN		6.58	91.46

### E. Effectiveness of the Multi-Scale Convolutional Block and Attention Mechanisms

To verify the effectiveness of the multi-scale convolutional block and attention mechanisms, we analyzed the proposed MSFCN without multi-scale convolutional block (MSFB), channel attention block (CAB) and global pooling module (GPM) both on WHDL and GID, and the results are shown in Table XIII and Table XIV.

TABLE XIII  
THE EFFECTIVENESS OF THE MULTI-SCALE CONVOLUTIONAL BLOCK AND ATTENTION MECHANISMS ON WHDL.

Method	OA	AA	K	mIoU	FWIoU	F1
U-Net	81.830	67.724	74.422	55.706	72.450	68.567
MSFB	82.708	68.301	75.459	57.098	73.119	69.941
MSFB+CAB	83.084	70.411	76.038	58.571	73.547	71.299
MSFB+GPM	83.433	70.214	76.608	58.608	74.347	71.003
MSFCN	84.168	72.081	77.558	60.366	74.892	73.031

The 3D U-Net obtains mIoU of 0.55706 and 0.69417 on WHDL and GID. When the conventional convolutional

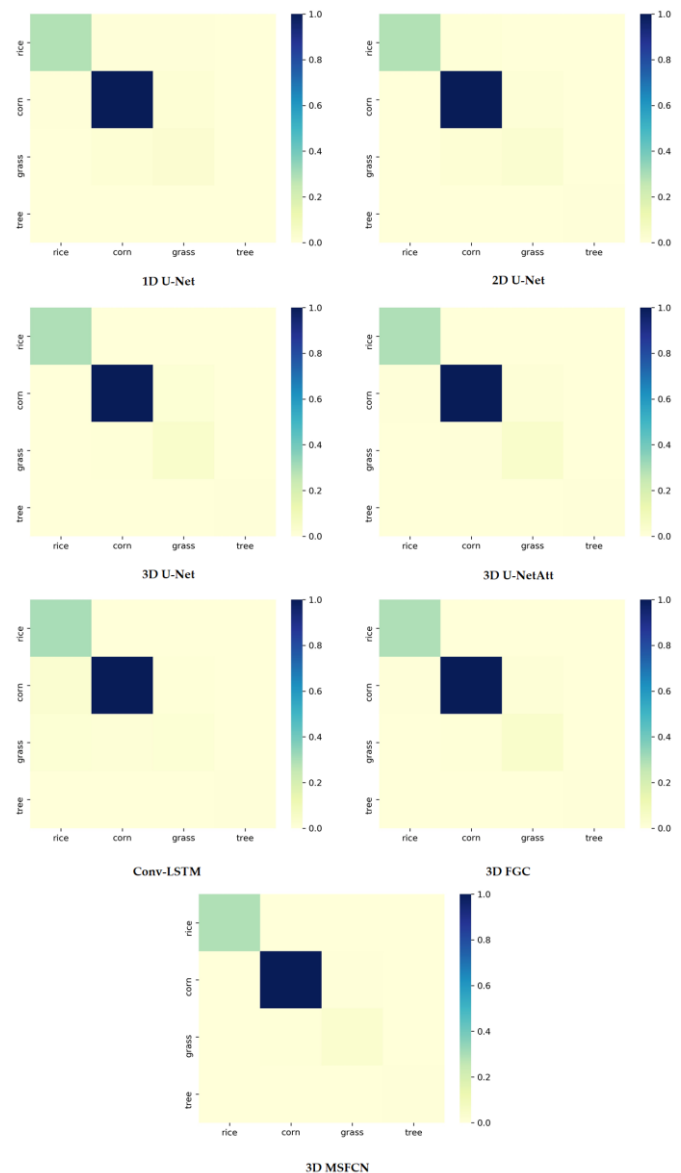


Fig. 15. Heat Maps of different methods on 2017 dataset.

TABLE XIV  
THE EFFECTIVENESS OF THE MULTI-SCALE CONVOLUTIONAL BLOCK AND ATTENTION MECHANISMS ON GID.

Method	OA	AA	K	mIoU	FWIoU	F1
U-Net	78.992	81.115	73.295	69.417	65.936	81.326
MSFB	81.579	83.429	76.620	71.992	69.715	83.276
MSFB+CAB	82.675	84.693	78.111	73.672	70.987	84.321
MSFB+GPM	82.891	84.136	78.302	73.671	71.575	84.453
MSFCN	83.718	85.544	79.353	75.127	72.688	85.378

blocks are replaced by multi-scale convolutional blocks, the mIoUs reach to 0.57098 and 0.71992. And the introduction of channel attention block and global pooling module brings 0.01473/0.01510 for WHDL and 0.01680/0.01679 for GID improvements on mIoU, respectively. The mIoUs are further improved to 0.60366 and 0.75127 when all blocks are introduced.

### F. Investigation about the Number of Layers and Channels

The number of layers and channels are two vital parameters which not only impact the performance of the model, but also

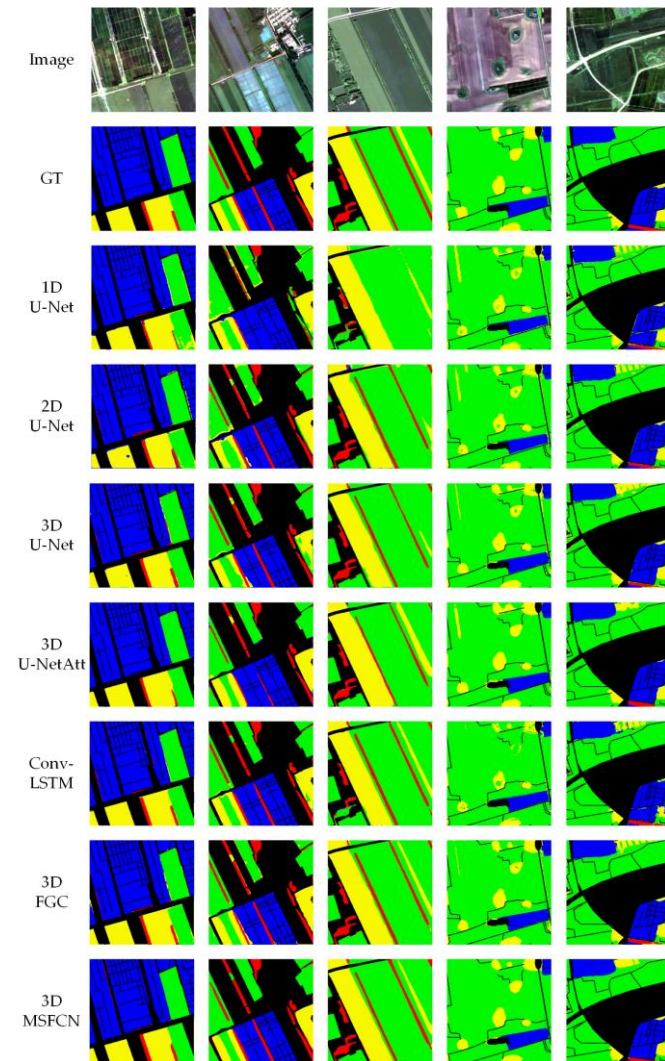


Fig. 16. Land cover classification results of the method proposed and comparisons on 2015 dataset and 2017 dataset.

determine the computational complexity. Thus, it is worthwhile to investigate the influence of the number of layers and channels.

To inquire the effect caused by the number of layers, we design a MSFCN with 3 layers (MSFCN3), and a MSFCN with 5 layers (MSFCN5), and compare their performance with the MSFCN with 4 layers (MSFCN4). As the capacity of representations is limited by finite layers, the performance of MSFCN3 is significantly weaker than MSFCN4. Specifically, without enormous increases in the parameters and computational complexity, MSFCN4 surpasses MSFCN3 more than 5% on mIoU, which can be seen from Table XV and Table XVII. However, notwithstanding certain improvements boosted by MSFCN5, the number of parameters of MSFCN5 is four times more than MSFCN4's, which is not an efficient option.

TABLE XV  
THE EFFECT CAUSED BY THE NUMBER OF LAYERS ON GID.

Method	OA	AA	K	mIoU	FWIoU	F1
MSFCN3	79.513	80.862	74.178	69.858	67.243	81.723
MSFCN4	83.718	85.544	79.353	75.127	72.688	85.378
MSFCN5	84.449	86.554	80.300	76.042	73.843	86.010

To research the impact caused by the number of channels, we design a narrow MSFCN (MSFCNN) with channels in the

TABLE XVI  
THE IMPACT CAUSED BY THE NUMBER OF CHANNELS ON GID.

Method	OA	AA	K	mIoU	FWIoU	F1
MSFCNN	80.218	83.652	70.530	70.530	67.529	82.104
MSFCN	83.718	85.544	79.353	75.127	72.688	85.378
MSFCNW	84.352	86.966	80.230	75.669	73.365	85.733

TABLE XVII  
THE COMPARISON OF PARAMETERS AND COMPUTATIONAL COMPLEXITY.

Method	input shape	Parameters (M)	Complexity (G)
MSFCN3		2.52	6.77
MSFCN4	3×256×256	2.67	9.66
MSFCN5		10.73	12.55
MSFCNN		0.67	2.46
MSFCN	3×256×256	2.67	9.66
MSFCNW		10.65	38.24

number of [16, 32, 64, 128], and a wide MSFCN (MSFCNW) with channels in the number of [64, 128, 256, 512], and compare their performance with the MSFCN with channels in the number of [32, 64, 128, 256]. The results show that the performance of MSFCN surpasses MSFCNN near 5% on mIoU. Meanwhile, with five times on parameters and computational complexity, MSFCNW just brings in near 1% improvement.

Based on the above experiments, we can draw a conclusion that the design of proposed MSFCN delicately balances the performance and complexity.

#### IV. CONCLUSION

In this paper, to implement land cover classification using satellite images, we propose a Multi-Scale Fully Convolutional Network (MSFCN). Firstly, multi-scale convolutional blocks are elaborately designed to expand the scope of information extraction in spatial domain, which captures both the local and global information of the satellite images. Secondly, a channel attention block and a global pooling module are included to enhance the channel consistency and global contextual consistency, respectively. Thirdly, we extend MSFCN to 3D for spatio-temporal satellite images based on 3D CNN to replace 2D FCN, which adequately utilizes the time series interaction of each land cover class on temporal dimension.

Experiments on two spatial datasets provide the effectiveness of proposed MSFCN. And experiments on two spatio-temporal datasets demonstrate the 3D CNN is a valid method to exploit information from spatio-temporal images. Meanwhile, we explore the impact caused by the number of layers and channels, which may provide beneficial references for designing land cover classification network based on FCN.

#### REFERENCES

- [1] J. Zhang, L. Feng, and F. Yao, "Improved maize cultivated area estimation over a large scale combining MODIS-EVI time series data and crop phenological information," *ISPRS J. Photogramm. Remote Sens.*, vol. 94, pp. 102-113, 2014.
- [2] B. Basso and L. Liu, "Seasonal crop yield forecast: Methods, applications, and accuracies," in *Advances in Agronomy*, vol. 154: Elsevier, 2019, pp. 201-255.
- [3] C. Zhang *et al.*, "A New CNN-Bayesian Model for Extracting Improved Winter Wheat Spatial Distribution from GF-2 imagery," *Remote Sens.*, vol. 11, no. 6, p. 619, 2019.
- [4] Y. Zhong, A. Ma, Y. soon Ong, Z. Zhu, and L. Zhang, "Computational intelligence in optical remote sensing image processing," *Appl. Soft Comput.*, vol. 64, pp. 75-93, 2018.

- [5] P. Wang, L. Zhang, G. Zhang, H. Bi, M. Dalla Mura, and J. Chanussot, "Superresolution land cover mapping based on pixel-, subpixel-, and superpixel-scale spatial dependence with pansharpening technique," *IEEE J. Sel. Top. Appl. Earth Obs. Remote Sens.*, vol. 12, no. 10, pp. 4082-4098, 2019.
- [6] G. Wang, J. Li, W. Sun, B. Xue, A. Yinglan, and T. Liu, "Non-point source pollution risks in a drinking water protection zone based on remote sensing data embedded within a nutrient budget model," *Water Res.*, vol. 157, pp. 238-246, 2019.
- [7] Z. Zhang, Y. Liu, T. Liu, Z. Lin, and S. Wang, "DAGN: A Real-Time UAV Remote Sensing Image Vehicle Detection Framework," *IEEE Geosci. Remote Sens. Lett.*, 2019.
- [8] C. Pelletier, G. I. Webb, and F. Petitjean, "Temporal convolutional neural network for the classification of satellite image time series," *Remote Sens.*, vol. 11, no. 5, p. 523, 2019.
- [9] Z. Xu, K. Guan, N. Casler, B. Peng, and S. Wang, "A 3D convolutional neural network method for land cover classification using LiDAR and multi-temporal Landsat imagery," *ISPRS J. Photogramm. Remote Sens.*, vol. 144, pp. 423-434, 2018.
- [10] C. J. Tucker, "Red and photographic infrared linear combinations for monitoring vegetation," 1978.
- [11] A. Huete, "Huete, AR A soil-adjusted vegetation index (SAVI). Remote Sensing of Environment," *Remote Sens. Environ.*, vol. 25, pp. 295-309, 1988.
- [12] H. Zhao and X. Chen, "Use of normalized difference bareness index in quickly mapping bare areas from TM/ETM+," in *International geoscience and remote sensing symposium*, 2005, vol. 3, p. 1666.
- [13] H. Li *et al.*, "Mapping urban bare land automatically from Landsat imagery with a simple index," *Remote Sens.*, vol. 9, no. 3, p. 249, 2017.
- [14] B.-C. Gao, "NDWI—A normalized difference water index for remote sensing of vegetation liquid water from space," *Remote Sens. Environ.*, vol. 58, no. 3, pp. 257-266, 1996.
- [15] H. Xu, "Modification of normalised difference water index (NDWI) to enhance open water features in remotely sensed imagery," *Int. J. Remote Sens.*, vol. 27, no. 14, pp. 3025-3033, 2006.
- [16] G. Rutherford, A. Guisan, and N. Zimmermann, "Evaluating sampling strategies and logistic regression methods for modelling complex land cover changes," *J. Appl. Ecol.*, vol. 44, no. 2, pp. 414-424, 2007.
- [17] Q. Du and C.-I. Chang, "A linear constrained distance-based discriminant analysis for hyperspectral image classification," *Pattern Recognit.*, vol. 34, no. 2, pp. 361-373, 2001.
- [18] U. Maulik and I. Saha, "Automatic fuzzy clustering using modified differential evolution for image classification," *IEEE Trans. Geosci. Remote Sens.*, vol. 48, no. 9, pp. 3503-3510, 2010.
- [19] Y. Fu *et al.*, "An improved combination of spectral and spatial features for vegetation classification in hyperspectral images," *Remote Sens.*, vol. 9, no. 3, p. 261, 2017.
- [20] K. Tatsumi, Y. Yamashiki, M. A. C. Torres, and C. L. R. Taípe, "Crop classification of upland fields using Random forest of time-series Landsat 7 ETM+ data," *Comput. Electron. Agric.*, vol. 115, pp. 171-179, 2015.
- [21] C. Adede, R. Oboko, P. W. Wagacha, and C. Atzberger, "A Mixed Model Approach to Vegetation Condition Prediction Using Artificial Neural Networks (ANN): Case of Kenya's Operational Drought Monitoring," *Remote Sens.*, vol. 11, no. 9, p. 1099, 2019.
- [22] C. Zhang *et al.*, "A hybrid MLP-CNN classifier for very fine resolution remotely sensed image classification," *ISPRS J. Photogramm. Remote Sens.*, vol. 140, pp. 133-144, 2018.
- [23] Z. Liu, P. Luo, X. Wang, and X. Tang, "Deep learning face attributes in the wild," in *Proceedings of the IEEE international conference on computer vision*, 2015, pp. 3730-3738.
- [24] J. Devlin, M.-W. Chang, K. Lee, and K. Toutanova, "Bert: Pre-training of deep bidirectional transformers for language understanding," *arXiv preprint arXiv:1810.04805*, 2018.
- [25] D. S. Park *et al.*, "SpecAugment: A simple data augmentation method for automatic speech recognition," *arXiv preprint arXiv:1904.08779*, 2019.
- [26] L. Zhong, L. Hu, and H. Zhou, "Deep learning based multi-temporal crop classification," *Remote Sens. Environ.*, vol. 221, pp. 430-443, 2019.
- [27] X.-Y. Tong *et al.*, "Land-cover classification with high-resolution remote sensing images using transferable deep models," *Remote Sens. Environ.*, vol. 237, p. 111322, 2020.
- [28] A. Stoian, V. Poulain, J. Inglada, V. Poughon, and D. Derksen, "Land cover maps production with high resolution satellite image time series and convolutional neural networks: Adaptations and limits for operational systems," *Remote Sens.*, vol. 11, no. 17, p. 1986, 2019.
- [29] K. Cao and X. Zhang, "An Improved Res-UNet Model for Tree Species Classification Using Airborne High-Resolution Images," *Remote Sens.*, vol. 12, no. 7, p. 1128, 2020.
- [30] O. Ronneberger, P. Fischer, and T. Brox, "U-net: Convolutional networks for biomedical image segmentation," in *International Conference on Medical image computing and computer-assisted intervention*, 2015: Springer, pp. 234-241.
- [31] V. Badrinarayanan, A. Kendall, and R. Cipolla, "Segnet: A deep convolutional encoder-decoder architecture for image segmentation," *IEEE Trans. Pattern Anal. Mach. Intell.*, vol. 39, no. 12, pp. 2481-2495, 2017.
- [32] L.-C. Chen, Y. Zhu, G. Papandreou, F. Schroff, and H. Adam, "Encoder-decoder with atrous separable convolution for semantic image segmentation," in *Proceedings of the European conference on computer vision (ECCV)*, 2018, pp. 801-818.
- [33] Q. Sang, Y. Zhuang, S. Dong, G. Wang, and H. Chen, "FRF-Net: Land Cover Classification From Large-Scale VHR Optical Remote Sensing Images," *IEEE Geosci. Remote Sens. Lett.*, 2019.
- [34] F. Mohammadimanesh, B. Salehi, M. Mahdianpari, E. Gill, and M. Molinier, "A new fully convolutional neural network for semantic segmentation of polarimetric SAR imagery in complex land cover ecosystem," *ISPRS J. Photogramm. Remote Sens.*, vol. 151, pp. 223-236, 2019.
- [35] Q. Liu, M. Kampffmeyer, R. Jenssen, and A.-B. Salberg, "Dense Dilated Convolutions' Merging Network for Land Cover Classification," *IEEE Trans. Geosci. Remote Sens.*, 2020.
- [36] S. Ji, Z. Zhang, C. Zhang, S. Wei, M. Lu, and Y. Duan, "Learning discriminative spatiotemporal features for precise crop classification from multi-temporal satellite images," *Int. J. Remote Sens.*, vol. 41, no. 8, pp. 3162-3174, 2020.
- [37] V. S. F. Garnot, L. Landrieu, S. Giordano, and N. Chehata, "Satellite Image Time Series Classification with Pixel-Set Encoders and Temporal Self-Attention," in *Proceedings of the IEEE/CVF Conference on Computer Vision and Pattern Recognition*, 2020, pp. 12325-12334.
- [38] M. Rußwurm and M. Körner, "Multi-temporal land cover classification with sequential recurrent encoders," *ISPRS Int. J. Geo-Inf.*, vol. 7, no. 4, p. 129, 2018.
- [39] M. Rußwurm and M. Korner, "Temporal vegetation modelling using long short-term memory networks for crop identification from medium-resolution multi-spectral satellite images," in *Proceedings of the IEEE Conference on Computer Vision and Pattern Recognition Workshops*, 2017, pp. 11-19.
- [40] R. Interdonato, D. Ienco, R. Gaetano, and K. Ose, "DuPLO: A Dual view Point deep Learning architecture for time series classificatiOn," *ISPRS J. Photogramm. Remote Sens.*, vol. 149, pp. 91-104, 2019.
- [41] R. M. Rustowicz, R. Cheong, L. Wang, S. Ermon, M. Burke, and D. Lobell, "Semantic segmentation of crop type in africa: A novel dataset and analysis of deep learning methods," in *Proceedings of the IEEE Conference on Computer Vision and Pattern Recognition Workshops*, 2019, pp. 75-82.
- [42] C.-Y. Wu, C. Feichtenhofer, H. Fan, K. He, P. Krahenbuhl, and R. Girshick, "Long-term feature banks for detailed video understanding," in *Proceedings of the IEEE Conference on Computer Vision and Pattern Recognition*, 2019, pp. 284-293.
- [43] H. Hamraz, N. B. Jacobs, M. A. Contreras, and C. H. Clark, "Deep learning for conifer/deciduous classification of airborne LiDAR 3D point clouds representing individual trees," *ISPRS J. Photogramm. Remote Sens.*, vol. 158, pp. 219-230, 2019.
- [44] Z. Gong *et al.*, "A Frustum-based probabilistic framework for 3D object detection by fusion of LiDAR and camera data," *ISPRS J. Photogramm. Remote Sens.*, vol. 159, pp. 90-100, 2020.
- [45] R. Li, S. Zheng, C. Duan, Y. Yang, and X. Wang, "Classification of Hyperspectral Image Based on Double-Branch Dual-Attention Mechanism Network," *Remote Sens.*, vol. 12, no. 3, p. 582, 2020.
- [46] S. Ji, C. Zhang, A. Xu, Y. Shi, and Y. Duan, "3D convolutional neural networks for crop classification with multi-temporal remote sensing images," *Remote Sens.*, vol. 10, no. 1, p. 75, 2018.

- [47] S. Jégou, M. Drozdal, D. Vazquez, A. Romero, and Y. Bengio, "The one hundred layers tiramisù: Fully convolutional densenets for semantic segmentation," in *Proceedings of the IEEE conference on computer vision and pattern recognition workshops*, 2017, pp. 11-19.
- [48] O. Oktay *et al.*, "Attention u-net: Learning where to look for the pancreas," *arXiv preprint arXiv:1804.03999*, 2018.
- [49] S. Ioffe and C. Szegedy, "Batch normalization: Accelerating deep network training by reducing internal covariate shift," *arXiv preprint arXiv:1502.03167*, 2015.
- [50] C. Yu, J. Wang, C. Peng, C. Gao, G. Yu, and N. Sang, "Bisenet: Bilateral segmentation network for real-time semantic segmentation," in *Proceedings of the European conference on computer vision (ECCV)*, 2018, pp. 325-341.
- [51] C. Yu, J. Wang, C. Peng, C. Gao, G. Yu, and N. Sang, "Learning a discriminative feature network for semantic segmentation," in *Proceedings of the IEEE conference on computer vision and pattern recognition*, 2018, pp. 1857-1866.
- [52] W. Liu, A. Rabinovich, and A. C. Berg, "Parsenet: Looking wider to see better," *arXiv preprint arXiv:1506.04579*, 2015.
- [53] Z. Shao, K. Yang, and W. Zhou, "Performance evaluation of single-label and multi-label remote sensing image retrieval using a dense labeling dataset," *Remote Sens.*, vol. 10, no. 6, p. 964, 2018.
- [54] Z. Shao, W. Zhou, X. Deng, M. Zhang, and Q. Cheng, "Multilabel Remote Sensing Image Retrieval Based on Fully Convolutional Network," *IEEE J. Sel. Top. Appl. Earth Obs. Remote Sens.*, vol. 13, pp. 318-328, 2020.
- [55] L. S. Bernstein *et al.*, "Validation of the QUick Atmospheric Correction (QUAC) algorithm for VNIR-SWIR multi-and hyperspectral imagery," in *Algorithms and Technologies for Multispectral, Hyperspectral, and Ultraspectral Imagery XI*, 2005, vol. 5806: International Society for Optics and Photonics, pp. 668-678.
- [56] M. Rußwurm, S. Wang, M. Korner, and D. Lobell, "Meta-Learning for Few-Shot Land Cover Classification," in *Proceedings of the IEEE/CVF Conference on Computer Vision and Pattern Recognition Workshops*, 2020, pp. 200-201.
- [57] H. Sheng, X. Chen, J. Su, R. Rajagopal, and A. Ng, "Effective Data Fusion with Generalized Vegetation Index: Evidence from Land Cover Segmentation in Agriculture," in *Proceedings of the IEEE/CVF Conference on Computer Vision and Pattern Recognition Workshops*, 2020, pp. 60-61.



**Rui Li** received the bachelor's degree in School of Automation Science and Engineering, South China University of Technology, Guangzhou, China in 2019. He is currently pursuing the master's degree with the School of Remote Sensing and Information Engineering, Wuhan University, Wuhan, China.

His research interests include hyperspectral image classification, machine learning, and deep learning.



**Chenxi Duan** received the bachelor's degree in College of Geology Engineering and Geomatics, Chang'an University, Xi'an, China in 2019. She is currently pursuing the master's degree with the State Key Laboratory of Information Engineering in Surveying, Mapping, and Remote Sensing, Wuhan University, Wuhan, China.

Her research interests include cloud removal, machine learning, and deep learning.



**Shunyi Zheng** received the Post-Doctorate from the State Key Laboratory of Information Engineering in Surveying, Mapping, and Remote Sensing, Wuhan University, Wuhan, China, in 2002. He is currently a Professor with School of Remote Sensing and Information Engineering, Wuhan University, Wuhan, China. His research interests include remote sensing data processing, digital photogrammetry and three-dimensional reconstruction.

Mr. Zheng's awards and honors include the First prize for scientific and technological progress in surveying and mapping 2012, the First prize for 2014

John I. Davidson President's Award, and the First prize for scientific and technological progress in surveying and mapping 20